Surface and shape modification of mackinawite (FeS) nanocrystals by cysteine adsorption: a first-principles DFT-D2 study

N. Y. Dzade,*[a] A. Roldan[b] and N. H. de Leeuw*[ab]

The control of nanoparticle shape offers promise for improving catalytic activity and selectivity through optimization of the structure of the catalytically active site. Here, we have employed density functional theory calculations with a correction for the long-range interactions (DFT-D2) to investigate the effect of adsorption of the amino acid cysteine on the {001}, {011}, {100}, and {111} surfaces of mackinawite, which are commonly found in FeS nanoparticles. We have calculated the surface energies and adsorption energies for all the surfaces considered, and compared the surface energies of the pure and adsorbed systems. Based on the calculated surface energies, we have simulated the thermodynamic crystal morphology of the pure and cysteine-modified FeS nanoparticles using Wulff's construction. The strength of cysteine adsorption is found to be related to the stability of different surfaces, where it adsorbs most strongly onto the least stable FeS{111} surface via bidentate Fe–S and Fe–N chemical bonds and most weakly onto the most stable FeS{001} surface via hydrogen-bonded interactions; the adsorption energy decreases in the order {111} 4 {100} 4 {011} 4 {001}. We demonstrate that the stronger binding of the cysteine to the {011}, {100}, and {111} surfaces rather than to the {001} facet results in shape modulation of the FeS nanoparticles, with the reactive surfaces more expressed in the thermodynamic crystal morphology compared to the unmodified FeS crystals. Information regarding the structural parameters, electronic structures and vibrational frequency assignments of the cysteine–FeS complexes is also presented.

1. Introduction

Nanoparticles have major impacts in fundamental research and many industrial applications due to their unique size- and shape-dependent properties such as electrical, magnetic, mechanical, optical and chemical properties, which largely differ from those of the bulk materials.[1–6] Because nanoparticles have different surface structures and thus different surface interactions com-pared to larger particles, they have an extremely high tendency toward adhesion and aggregation.[2] It is therefore important to develop synthesis techniques to control the dispersion or aggregation of nanoparticles which dictate their crystal shape. Control of nanocrystal shape is important in various applications, such as in heterogeneous catalysis,[7,8] solar cells,[9] light-emitting diodes,[10,11] and biological labeling.[12,13] In particular, it offers promise for improving catalytic activity and selectivity through optimization of the structure of the catalytically active site. Simultaneous control of size, morphology, and size distribution of colloidal nanocrystals is however, a challenging task.

Generally, the synthesis of nanoparticles involves surfactant molecules that bind to their surface, which stabilize the nuclei and larger nanoparticles against aggregation by a repulsive force between the adsorbates, which controls the growth of nanoparticles in terms of the rate, final size or geometric shape. The surfactant/capping molecules also improve the stability of the nanoparticles against temperature and possible oxidation that could result in their degradation.[14,15] Depending on the nanoparticle material and surfactant molecules used, shape controlled growth is also possible, e.g. by stronger binding of the ligand to certain crystal facets.[1,2,15–19] The ligand molecules bound to the nanoparticle surface via the head group not only control the growth of the particles during synthesis, but also prevent the aggregation of the nanoparticles. Various chemical functional groups possess certain affinity to inorganic surfaces, the most famous example being the affinity of thiol to gold.[2,20] The possible choice of ligand molecules can depend on the material of the nanoparticle core, the particle size and the solvent. Generally, it is found that strongly binding molecules forming a dense layer stabilize the particles better than the

[a]Department of Earth Sciences, Utrecht University, Princetonplein 9, 3584 CC, Utrecht, The Netherlands. E-mail: N.Y.Dzade@uu.nl, N.H.Deleeuw@uu.nl

[b]School of Chemistry, Cardiff University, Main Building, Park Place, CF10 3AT, Cardiff, UK

weakly binding ones, and particularly, if further processing and purification steps are required after the particle synthesis.[20]

The synthesis and characterization of transition metal chalcogenide nanocrystals have become of interest fairly recently as they possess germane properties for many applications including in solar cells,[21–25] solid state batteries,[26–29] biomedicine,[30,31] and heterogeneous catalysis.[32–37] Variously shaped transition metal chalcogenide nanocrystals can be synthesized by using suitable reducing agents and surface-capping agents.[38–44] For example, capping agents such as long-chain amines and L-cysteine are often dissolved in the synthesis solution to prevent the aggregation of iron sulfide nanoparticles.[38–41] Many biological molecules have also been used either in the synthesis or capping of CdS nanoparticles.[42–44] Cysteine and thiolates, which are able to form high-affinity metal ligand clusters, have been shown to promote the formation of CdS and ZnS nanocrystals.[42–44] Further control over nanocrystal synthesis has been gained by using fatty acids, which have been found to promote the formation of CdSe and CdS nanocrystals.[45]

Modifying the surface of mackinawite (tetragonal iron(II) sulfide) nanoparticles by L-cysteine has been shown to modulate the shape and make it more resistant to oxidation.[46] Mackinawite crystallises in the tetragonal structure, with the space group P4/nmm.[47,48] The FeS structure is formed by vertically stacked two-dimensional (2D) layers with strong covalent bonding between Fe and S atoms within a given layer and very weak van der Waals bonding between the adjacent layers (Fig. 1a). Mackinawite (FeS) and greigite (Fe_3S_4) are increasingly considered to be the pre-biotic catalysts for a series of biochemical reactions that occur in hydrothermal systems, making them relevant to the origin of life theories.[32–35,49–51]

Experimentally, it is often difficult to determine the funda-mental interactions that take place between surfaces and the functional groups of the surfactants, which are thought to be the main contributing factors in the capping process.[20] However, using simulation techniques capable of modelling the structure of mineral surfaces at the atomic level, it is possible to study computationally the interactions between the crystal surface and the adsorbates. Several reviews and articles are available in the literature on the adsorption of amino acids on mineral surfaces, particularly with regard to the origin of life on Earth,[60–69] and on metallic surfaces.[58,70–72] However, investigations of cysteine adsorption have revealed a complex scenario in which it is hard to identify a unique bonding paradigm due to different functional groups in cysteine (thiol, amine, and carboxyl) that can interact with the mineral or metal surface. It appears that, depending on several experimental conditions, the interactions may vary sub-stantially and even exhibit different configurations. The picture that has emerged so far from experimental and theoretical investigations is that the cysteine molecule interacts with the metal via either the thiol (–SH)[52–54] or the amine ($–NH_2$)[55] side groups. Additionally, the –COOH end group might also interact with the surface. When all three functional groups of cysteine are free and not engaged in other biochemical interactions, the molecule can bind to metal/mineral surfaces by employing more than one end group.[56] The interactions of the thiol group can be easily identified by Fourier transform infrared spectroscopy (FT-IR), the spectrum showing the vanishing of the stretching S–H band at 2562 cm^{-1}.[57–60]

In this study, we have used density functional theory calculations, corrected for dispersion-interactions (DFT-D2), to investigate the adsorption of the amino acid cysteine on the low-index {001}, {011}, {100} and {111} surfaces of mackinawite. Electronic structure calculations based on DFT techniques have become indispensable in unravelling the interactions of organic molecules with solid surfaces as they are capable of accurately predicting the lowest-energy adsorption geometries and identifying the charge transfer and other electronic effects.[73,74] We have considered different coupling schemes that involve one or more functional groups of the cysteine molecule and report the analyses of the structures and energetics of different optimized adsorption configurations. The binding strengths, electronic structures and vibrational properties of the cysteine–FeS complexes are discussed. Finally, using Wulff's construction,[75] we have simulated the thermodynamic crystal morphology of the FeS nanoparticle based on the calculated surface energies before and after cysteine adsorption.

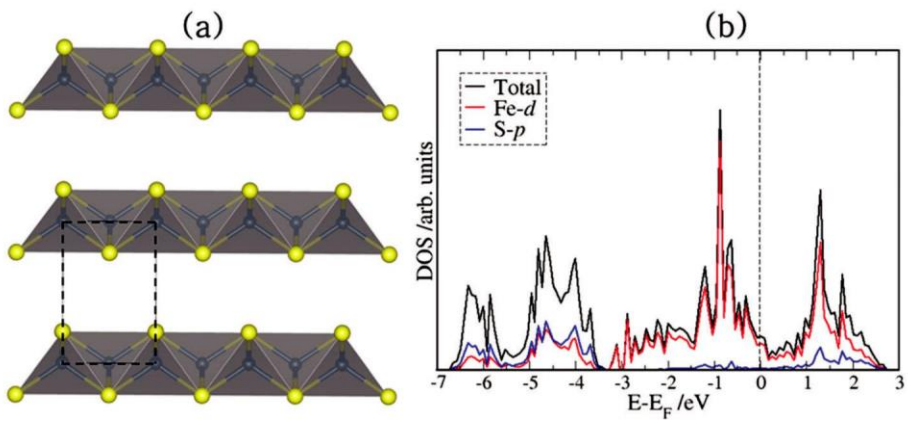

Fig. 1 (a) The layered structure of mackinawite, with the tetragonal unit cell highlighted by dashed lines. (b) The electronic density of states showing the total and projected values on the Fe d-states and S p-states (colour scheme: Fe = grey, S = yellow).

2. Computational details

The relaxed structures and energies were determined using plane-wave density functional theory (PW-DFT) calculations within the Vienna Ab initio Simulation Package (VASP).[76–78] Long-range dispersion forces were accounted for in our calcula-tions using the DFT-D2 approach of Grimme,[79] which is essential for an accurate description of the FeS interlayer interactions, as well as the interactions between the cysteine and FeS surfaces.[33,34,80] The electronic exchange–correlation potential was calculated using the generalized gradient approximation (GGA), with the PW91 functional.[81,82] The inter-actions between the valence electrons and the core were described with the projected augmented wave (PAW) method[83] in the implementation of Kresse and Joubert.[84] A plane-wave basis with an energy cut-off of 400 eV was tested to be sufficient to converge the total energy of mackinawite to within 0.0001 eV. Integration over the Brillouin zone is carried out using the Monkhorst–Pack scheme[85] with 11 11 11 and 5 5 1 meshes of k-points for bulk and surface calculations, respectively. Geometry optimizations were performed using the conjugate gradient minimization algorithm until the magnitude of the residual Hellman–Feynman force on each relaxed atom reached 0.01 eV Å ^{1}. The resulting cell parameters were a = 3.587 Å, c = 4.908 Å, and c/a = 1.368 Å,[34,34,80] which compare closely with those measured experimentally (a = 3.674 Å, c = 5.033 Å, and c/a = 1.370 Å).[47,48] The metallic character of FeS is also accurately reproduced as shown in Fig. 1b, with the electronic states of the Fe d-orbitals dominating the regions around the Fermi level, in agreement with the metallic nature deduced by Vaughan and Ridout,[87] and previous DFT results.[86,88,89]

The {001}, {011}, {100} and {111} surfaces were considered for the cysteine adsorption calculations as they are the domi-nant growth surfaces of FeS nanocrsytals.[90] These surfaces were created from the fully relaxed bulk using the METADISE code,[91] which not only considers periodicity in the plane direction but also provides diff erent atomic layer stacks resulting in a zero dipole moment perpendicular to the surface plane, as is required for reliable and realistic surface calculations.[92] A vacuum region of 15 Å was tested to be sufficient to avoid interactions between periodic slabs. Fig. 2 shows the top views of the relaxed structures of the most stable terminations of each FeS surface, where the {001} and the {111} surfaces are termi-nated by S, {011} is an Fe-termination, and the {100} termina-tion contains both S and Fe in the surface plane. The cysteine adsorption calculations were carried out on large surface slabs constructed from (3 3) of the {001} unit cell and (4 2) of the {011}, {100} and {111} unit cells. These simulation supercells are large enough to minimize the lateral interaction between the cysteine molecules in neighbouring image cells. The struc-tural optimizations of the FeS–cysteine systems were carried out without any symmetry constraint, and in particular, the cysteine molecule was free to move away laterally and vertically from the initial binding site or reorient itself to find the minimum energy adsorption structure. All atoms of the cysteine molecule and the topmost three atomic layers of the surface slabs

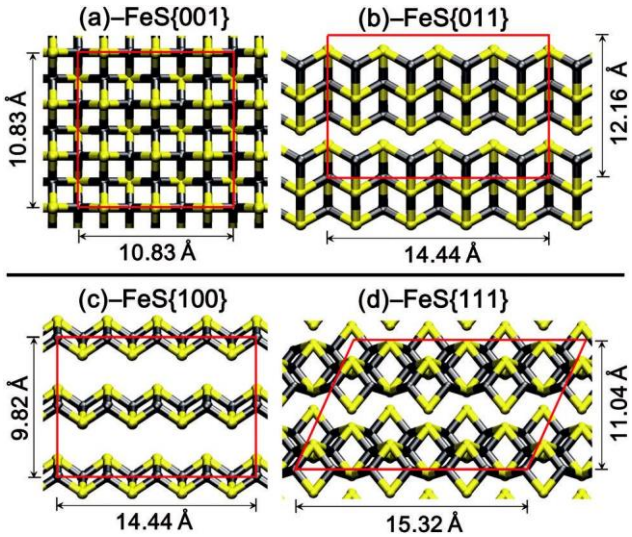

Fig. 2 Top views of the relaxed structures of (a) FeS{001}, (b) FeS{011}, (c) FeS{100}, and (d) FeS{111}surfaces used for the adsorption of cysteine (colour scheme: Fe = grey, S = yellow). The size of the simulation cells is highlighted by continuous red lines.

were allowed to relax unconstrainedly until residual forces on all atoms reached 0.01 eV Å ^{1}.

The adsorption energy (E_{ads}) which is a measure of the strength of the FeS–cysteine interaction is defined as follows:

$$E_{ads} = E_{surface+cysteine} - (E_{surface} + E_{cysteine}) \quad (1)$$

where $E_{surface+cysteine}$ is the total energy of the FeS–cysteine system in the equilibrium state, $E_{surface}$ is the total energy of the relaxed FeS surface slab alone, and $E_{cysteine}$ is the total energy of free cysteine in the gas phase. By this definition, a negative value of E_{ads} corresponds to an exothermic and favourable adsorption process. In this work, all of the reported adsorption energies were corrected by the zero-point energy (DZPE) calculated as the difference between the ZPE correction of the adsorbate on the surface and in the gas phase according to eqn (2):

$$DZPE = \left[\sum_{i=1}^{3n} \frac{h\nu_i}{2}\right]_{surf} - \left[\sum_{i=1}^{3n} \frac{h\nu_i}{2}\right]_{gas} \quad (2)$$

where h is the Planck constant and ν_i's are the vibrational frequencies. Vibrational frequency calculations were performed within the framework of the self-consistent density functional perturbation theory (DFTP).[93] The implementation of harmonic DFPT in a plane-wave pseudopotential framework presents several advantages. The main advantage of harmonic DFPT over other methods for computing vibrations of crystalline solids is that the responses to perturbations of different wave-lengths are decoupled. Thus, vibrational frequencies $\omega_i(q)$ can be calculated at any arbitrary wave vector q, avoiding the use of large supercells as required in standard methods, which calcu-late only zone-centered (G-point) frequencies. Also, plane waves are particularly convenient in a DFPT implementation for rapid exchanges between reciprocal and real spaces by fast Fourier

transform, for precision regulated by the size of the basis set and for derivative calculation of the Hellmann–Feynman forces and force constants without any Pulay correction. More infor-mation regarding the DFTP approach and its mathematical formulation can be found in the review paper (Phonons and related crystal properties from density-functional perturbation theory) by Baroni et al.[93]

The equilibrium morphologies of the FeS crystal before and after cysteine adsorption are determined from the relaxed surface energies of the various surfaces, which provide a measure of the relative stabilities of the surfaces. The equili-brium morphology is constructed according to Wulff's theorem,[75] which states that a polar plot of surface energy versus the orientation of normal vectors would give the crystal morphology based on the approach of Gibbs.[94] According to the Gibbs formulation, under thermodynamic conditions, the equi-librium shape of a crystal should possess minimal total surface free energy for a given volume.

The surface energy of the unrelaxed surfaces (γ_u) was derived from a single point calculation of the pure symmetric stoichio-metric slab before relaxation, via the equation:

$$\gamma_u = \frac{E_{slab}^{unrelaxed} - nE_{bulk}}{2A} \quad (3)$$

where $E_{slab}^{unrelaxed}$ is the energy of the unrelaxed slab, nE_{bulk} is the energy of an equal number (n) of the bulk FeS atoms, and A is the area of one side of the slab. During relaxation, the top surface was allowed to relax and the bottom one was kept fixed. The additional energy due to the relaxed surface at the top of the slab must be separated from the energy of the unrelaxed surface at the bottom, as the two differ. From the unrelaxed surface energy it is possible to calculate the relaxed surface energy (γ_r) from the total energy of the relaxed slab as:

$$\gamma_r = \frac{E_{slab}^{relaxed} - nE_{bulk}}{A} - \gamma_u \quad (4)$$

where $E^{relaxed}_{slab}$ is the energy of the relaxed slab. Considering that the adsorption of cysteine on the FeS surfaces changes the surface energies and therefore may alter the equilibrium mor-phology, we have also calculated the surface energies of the surfaces after cysteine adsorption using eqn (5):

$$\gamma_{cysteine} = \frac{E^{relaxed}_{slab+cysteine} - nE_{cysteine} - nE_{bulk}}{A} - \gamma_u \quad (5)$$

where $E^{relaxed}_{slab+cysteine}$ is the energy of the surface with adsorbed cysteine and $nE_{cysteine}$ is the energy of an equivalent number of free cysteine molecules in the gas phase.

3. Results and discussion

3.1 Cysteine molecule in the gas phase

To ensure that our calculations are of sufficiently high accuracy, we first compared our calculated structural parameters of the free cysteine molecule with those of available theoretical[72,95] and experimental X-ray[96,97] and neutron diffraction[98] data. The fully relaxed structure of cysteine is shown in Fig. 3a and the calculated bond distances and angles are summarized in Table 1, showing good agreement with experimental data[96–98] and earlier DFT-PW91[72] and semiempirical-PM3[95] calculations. Any differences compared to the experimental data are likely due to the fact that the optimization was performed under isolated conditions, whereas the crystal environment will have affected the experimental X-ray and neutron diffraction struc-tures. We have also determined the highest occupied molecular

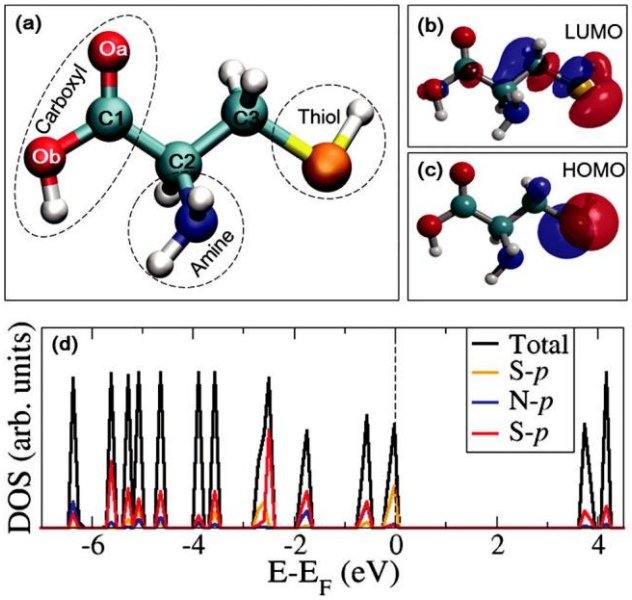

Fig. 3 Schematic representation of (a) the optimized structure, (b) the lowest unoccupied molecular orbital (LUMO), (c) the highest occupied molecular orbital (HOMO) and (d) the projected density of states (PDOS) of cysteine. The three potential surface-binding groups are highlighted in dashed circles (colour scheme: O = red, C = green, S = orange and H = white).

Table 1 The equilibrium structural parameters of cysteine calculated in this work and compared with available experiment data

Parameter	This work	PW91[72]	PM3[95]	X-ray[96]	X-ray[97]	Neutron[98]
Bond distance (Å)						
d(C_1–O_a)	1.212	1.230	1.218	1.208	1.260	1.251
d(C_1–O_b)	1.369	1.370	1.350	1.338	1.250	1.239
d(O_b–H)	0.977	—	0.952	0.972	—	—
d(C_1—C_2)	1.525	1.520	1.527	1.509	1.530	1.530
d(C_2—C_3)	1.531	1.550	1.536	1.523	1.530	1.530
d(C_2—H)	1.104	—	1.122	1.113	—	1.104
d(C_3—H)	1.095	—	1.107	1.113	—	1.077
d(C_2—N)	1.465	1.470	1.483	1.468	1.483	1.488
d(N—H)	1.022	—	0.998	1.035	—	1.038
d(C_3—S)	1.822	1.860	1.815	1.815	1.819	1.800
d(S—H)	1.350	—	1.307	1.345	1.340	1.270
Bond angle (1)						
a(C_2—C_1—O_a)	125.0	124.6	128.6	122.5	118.1	117.3
a(C_2—C_1—O_b)	115.3	113.1	115.0	107.1	116.7	117.0
a(O_a—C_1—O_b)	123.6	122.3	116.4	122.0	125.3	125.7
a(C_1—C_2—C_3)	111.0	111.3	110.6	109.9	111.7	111.1
a(C_1—C_2—N)	110.4	109.1	106.7	110.7	109.9	111.1
a(C_3—C_2—N)	110.1	109.3	113.7	108.8	111.3	110.9
a(C_2—C_3—S)	114.5	116.8	114.9	106.5	115.1	114.8
a(C_3—S—H)	96.2	—	100.5	96.0	98.1	97.0

orbital (HOMO) and the lowest unoccupied molecular orbital (LUMO) of cysteine and presented them, respectively, in Fig. 3b and c. Both the HOMO and the LUMO are dominated by the 3p character of the sulfur atom which is expected to play a vital role in the interaction of cysteine with the given FeS surfaces, as has been seen on metallic surfaces.[67–70] Similarly, the projected density of states (PDOS) as displayed in Fig. 3d reveals that the states at the Fermi level are dominated by S p-states, and these orbitals are expected to play an important role in the binding of the cysteine molecule to the FeS surfaces.

3.2 Cysteine adsorption on FeS{001}

Cysteine has three potential metal-binding groups; the thiol (–SH), amine ($–NH_2$), and carboxyl (–COOH) end groups (Fig. 3a), and it may thus act as a monodentate, bidentate, or tridentate ligand. In order to determine the preferred adsorp-tion sites and binding modes of cysteine on the {001} surface, we optimized the cysteine molecule from a number of different initial orientations on the surface, without any symmetry constraints. The optimized adsorption structures are shown in Fig. 4 and the calculated adsorption energies and any charge transferred to the adsorbed cysteine molecule are listed in Table 2. All four identified adsorption modes gave similar exo-thermic energies, with the strongest adsorption at 0.70 eV, calculated for the flat adsorption configuration (Fig. 4a). The adsorption energy of the flat configuration is comparable to 0.65 eV for the SH-end configuration (Fig. 4b), 0.63 eV for CH–N-end (Fig. 4c), and 0.57 eV for the Oa-end configuration (Fig. 4d). In the flat adsorption configuration (Fig. 4a), the cysteine molecule lies almost flat on the surface with the hydrogen atoms from the three end-groups pointing towards the surface sulfur atoms in such a manner that the interatomic distances between the hydrogen atoms of the carboxyl, thiol, and amine groups and the surface sulfur atoms are calculated at 2.382 Å, 2.571 Å, and 2.700 Å, respectively. Similar S–H interatomic distances are obtained for the SH-end, CH–N-end, and Oa-end configurations, which are calculated at 2.57 Å, 2.96 Å, and 3.21 Å, respectively (see Fig. 4). These adsorption modes suggest very weak hydrogen-bonded interactions between the cysteine molecule and the surface sulfur atoms, considering that the H–surface distances are larger than the typical hydrogen-bond length in water, which is 1.97 Å.[99] It therefore suggests that van der Waals interactions (vdW) play an important role in stabilizing the adsorbed cysteine molecule on the {001} surface. The contribution of the van der Waals interactions (E_{vdW}) to the adsorption energy for the flat, SH-end, CH–N-end, and Oa-end configurations is calculated at 0.37, 0.30, 0.27 and 0.25 eV, respectively. In all four adsorption configurations on the {001} surface, we found that the structural parameters of cysteine are not significantly affected by the adsorption process, which is consistent with the

Table 2 Adsorption energies (E_{ads}) and the relevant bond distances of cysteine adsorbed onto the {001}, {011}, {100} and {111} FeS surfaces. |q| denotes the net charge gained by the cysteine molecule

Surface	Config.	E_{ads} (eV)	d(Fe–S) (Å)	d(Fe–N) (Å)	d(Fe–O) (Å)	|q| (e)
FeS{001}	Flat	0.60	4.694	4.502	4.307	0.01
	SH-end	0.57	4.899	—	4.283	0.00
	CH–N-end	0.52	—	4.468	—	0.00
	O_a-end	0.49	—	—	3.726	0.00
FeS{011}	Fe–NS–Fe	1.861	2.382	2.163	—	0.16
	Fe–S	1.622	2.343	—	—	0.05
	Fe–N	1.426	—	2.102	—	0.04
	Fe–OO–Fe	0.995	—	—	2.093	0.03
FeS{100}	Fe–NS–Fe	2.26	2.380	2.140	—	0.01
	Fe–N	1.65	—	2.084	—	0.00
	Fe–O	0.98	—	—	2.001	0.00
FeS{111}	Fe–NS–Fe	3.41	2.264	2.130	—	0.16
	Fe–S–Fe	2.48	2.123	—	—	0.05
	Fe–OO–Fe	2.05	—	2.084	2.183	0.04
	Fe–N	1.79	—	2.102	—	0.03

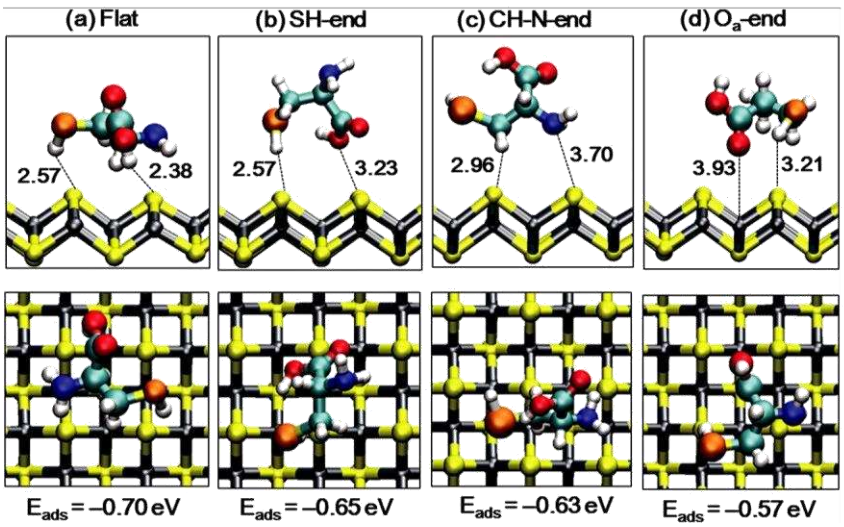

Fig. 4 The lowest-energy adsorption configurations of cysteine on the FeS{001} surface, in side (top) and top (bottom) views. Distances in Angstroms (Å). (colour scheme: Fe = grey, $S_{surface}$ = yellow, $S_{molecule}$ = orange; O, C, N and H are the same as in Fig. 3).

Table 3 Structural parameters (bond distances and angles) of cysteine adsorbed onto FeS{001} and FeS{011} surfaces

	FeS{001}				FeS{011}			
Parameter	Flat	SH-end	CH–N-end	O_a-end	Fe–NS–Fe	Fe–OO–Fe	Fe–S	Fe–N
Distance (Å)								
d(C_2–N)	1.469	1.465	1.458	1.450	1.495	1.474	1.420	1.503
d(C_3–S)	1.823	1.829	1.839	1.827	1.844	1.830	1.840	1.823
d(C_1–O_a)	1.211	1.216	1.216	1.217	1.211	1.234	1.216	1.213
d(C_1–O_b)	1.368	1.363	1.357	1.367	1.367	1.379	1.356	1.362
d(C_1–C_2)	1.537	1.540	1.544	1.535	1.531	1.519	1.533	1.529
d(C_2–C_3)	1.527	1.530	1.546	1.528	1.525	1.525	1.535	1.518
d(S–H)	1.351	1.352	1.350	1.351	1.354	1.349	1.359	1.359
d(O–H)	0.984	0.980	0.992	0.977	0.980	0.979	0.994	0.993
d(C_2–H)	1.109	1.102	1.105	1.103	1.108	1.105	1.103	1.102
d(N–H)	1.022	1.023	1.024	1.0.22	1.026	1.022	1.022	1.026
Angle (1)								
a(C_1–C_2–C_3)	110.8	108.7	112.3	110.8	112.8	109.2	108.1	113.7
a(C_1–C_2–N)	108.3	111.5	113.2	110.7	110.8	112.7	114.5	108.1
a(C_3–C_2–N)	109.1	109.3	107.7	108.8	110.6	110.9	109.8	110.6
a(C_2–C_1–O_a)	125.1	122.1	123.2	123.8	125.5	125.8	123.0	125.0
a(C_2–C_1–O_b)	114.6	117.9	115.9	116.4	113.7	114.8	115.9	113.7
a(O_a–C_1–O_b)	120.3	119.9	120.9	119.6	120.8	119.4	121.0	121.1
a(C_2–C_3–S)	113.7	113.0	116.6	114.7	106.8	110.1	106.4	111.1
a(C_3–S–H)	96.9	95.8	97.3	95.3	96.8	95.3	96.5	95.5

fairly weak adsorption energies calculated on this surface. Reported in Table 3 are the internal bond distances and angles of the adsorbed cysteine, which remained similar to those calculated for the gas phase molecule.

3.3 Cysteine adsorption on FeS{011}

As on the {001} surface, we have optimized a number of different initial orientations of the cysteine molecule on the {011} surface without any symmetry constraints, in order to determine the preferred adsorption sites and the lowest-energy adsorption structures. Four different adsorption modes including two bidentate configurations, wherein the cysteine binds at Fe sites either via the –COOH end forming two Fe–O bonds (denoted Fe–OO–Fe) or via the $–NH_2$ and –SH end groups forming Fe–N and Fe–S bonds (denoted Fe–NS–Fe), and two monodentate configurations, wherein the cysteine is adsorbed via only the –SH end group (denoted Fe–S) or $–NH_2$ end group (denoted Fe–N), were considered. The relaxed cysteine/FeS{011} adsorp-tion structures are shown in Fig. 5, whereas the calculated adsorption energies and structural parameters, including bond distances and angles, are reported in Tables 2 and 3. The strongest adsorption is computed for the Fe–NS–Fe configu-ration with an adsorption energy of 1.86 eV, compared to 1.62 eV for Fe–S, 1.43 eV for Fe–N and 0.99 eV for the Fe–OO–Fe configurations. Compared to the {001} surface, the contribution of the van der Waals interactions to the adsorption energy is smaller, which is calculated at 0.23, 0.20, 0.17 and 0.11 eV for the Fe–NS–Fe, Fe–S, Fe–N, and Fe–OO–Fe configurations, respectively. The adsorption energies on the {011} surface are larger than the ones obtained on the

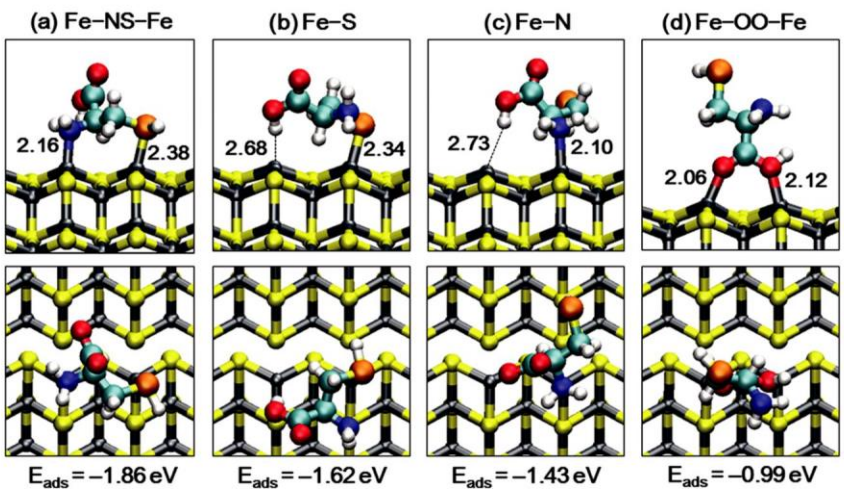

Fig. 5 The lowest-energy adsorption configurations of cysteine on the FeS{011} surface, in side (top) and top (bottom) views. Distances in Angstroms (Å). (colour scheme: Fe = grey, $S_{surface}$ = yellow, $S_{molecule}$ = orange; O, C, N and H are the same as in Fig. 3).

{001} surface, indicating a stronger interaction of the cysteine with the {011} surface than with the {001} surface. The stronger interaction on the {011} surface can be attributed to the direct molecule–cation interactions, which are absent on the {001} surface, as the layer of negatively charged S ions shields the inner Fe ions. In the lowest-energy complex (Fe–NS–Fe), the Fe–S and Fe–N bond distances are calculated at 2.379 Å and 2.158 Å respectively, which are comparable to the distances of 2.341 Å and 2.082 Å in the monodentate Fe–S and Fe–N binding modes, respectively. For the bidentate Fe–OO–Fe configuration, the O_a–Fe and O_b–Fe bond distances are, respectively, calcu-lated at 2.068 Å and 2.125 Å. Our calculated Fe–S interatomic distances on the FeS{011} surface are shorter than the value of 2.510 Å reported for Au–S on Au{111}[72] and for other thiols at the bridge (2.50 Å) and at the fcc (2.52 Å) sites of Au{111}.[100,101] Shown in Table 3 are the calculated internal bond distances and bond angles of the adsorbed cysteine on the {011} surface. When compared to the gas phase geometries, we observe a small difference that can be attributed to the stronger cysteine– surface interactions calculated on this surface.

3.4 Cysteine adsorption on FeS{100}

Similar to the {011} surface, we have optimized a number of diff erent initial orientations of the cysteine molecule on the {100} surface without any symmetry constraints, in order to determine the preferred adsorption sites and the lowest-energy adsorption configurations. We found three stable adsorption configurations (Fig. 6), wherein the cysteine adsorbs onto Fe sites either via both the $–NH_2$ and –SH end groups forming Fe–N and Fe–S bonds (Fe–NS–Fe) or via only the $–NH_2$ end group (denoted Fe–N) or the –COOH end group (denoted Fe–O). The calculated adsorption energies and structural parameters, including bond distances and angles, are reported in Tables 2 and 4. The strongest adsorption is computed for the Fe–NS–Fe configu-ration which released an adsorption energy of 2.26 eV (E_{vdW} = 0.37 eV), compared to 1.65 eV (E_{vdW} = 0.23 eV) for Fe–N and 0.98 eV (E_{vdW} = 0.21 eV) for the Fe–O configurations. In the lowest-energy Fe–NS–Fe configuration, the Fe–S and Fe–N bond distances are calculated at 2.380 Å and 2.140 Å, respectively, which are shorter than those obtained at the FeS{011} surface (Table 2), thus indicating stronger adsorption on FeS{100} than on FeS{011}. We observed that the adsorption of cysteine on the FeS{100} surface results in layer expansion, particularly in the Fe–NS–Fe and Fe–N configurations where the cysteine interacts across layers. The space between the layers (d_{001}) increased from 4.908 in the naked surface to 5.331 Å, 5.220 Å, and 5.056 Å after cysteine adsorption in the Fe–NS–Fe, Fe–N, and Fe–O configurations, respectively. A similar layer space expansion was observed in synthetic poorly crystallized FeS samples, with the layer spacing reported to be 5.24 Å and 5.49 Å for the unmodified FeS and cysteine modified FeS particles, respectively.[46] The strong adsorption of the cysteine molecule on the FeS{100} also gave rise to changes in the internal bond distances and bond angles (Table 4) and vibration modes (Table 7) when compared to the gas phase geometries.

3.5 Cysteine adsorption on FeS{111}

The representative lowest-energy adsorption structures of cysteine on the FeS{111} surface are shown in Fig. 7 with the energetics and structural details listed in Tables 2 and 4 respectively. We found the strongest adsorption on FeS{111} when cysteine binds via –SH and $–NH_2$ end groups forming bidentate Fe–S and Fe–N bonds (Fe–NS–Fe, Fig. 7a), with an adsorption energy of 3.42 eV (E_{vdW} = 0.47 eV). When compared to the adsorption energy released in the lowest-energy structures on the other surfaces (Table 2), it can be concluded that FeS{111} is the most reactive surface towards cysteine adsorption. Consistent with its superior reactivity towards cysteine adsorption, shorter Fe–S (2.264 Å) and Fe–N (2.130 Å) are calculated on FeS{111} for the Fe–NS–Fe configu-ration compared to the other surfaces (Table 2). A strong adsorption is also obtained when the –SH end group of the cysteine molecule bridges between two surface Fe ions at Fe–S distances of 2.102 Å and 2.140 Å, with an adsorption energy of 2.48 eV (E_{vdW} = 0.34 eV). The bidentate Fe–OO–Fe and the

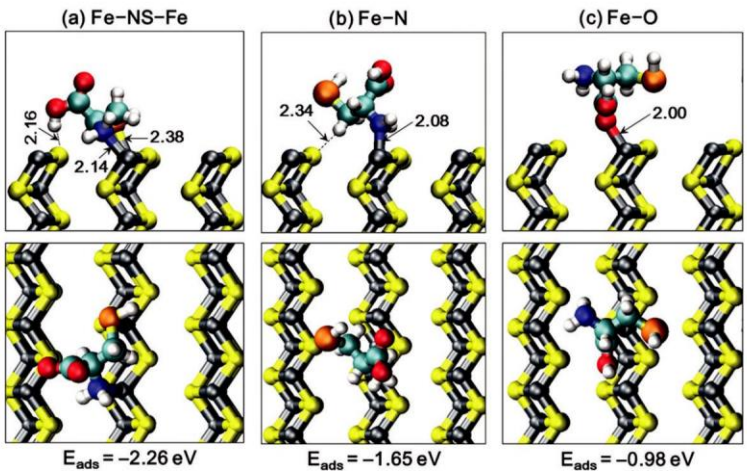

Fig. 6 The lowest-energy adsorption configurations of cysteine on the FeS{100} surface, in side (top) and top (bottom) views. Distances in Angstroms (Å). (colour scheme: Fe = grey, $S_{surface}$ = yellow, $S_{molecule}$ = orange; O, C, N and H are the same as in Fig. 3).

Table 4 Structural parameters (bond distances and angles) of cysteine adsorbed onto FeS{100} and FeS{111} surfaces

	FeS{100}			FeS{111}			
Parameter	Fe–NS–Fe	Fe–N	Fe–O	Fe–NS–Fe	Fe–S–Fe	Fe–OO–Fe	Fe–N
Distance (Å)							
d(C_2–N)	1.492	1.486	1.459	1.500	1.449	1.460	1.500
d(C_3–S)	1.835	1.826	1.830	1.865	1.851	1.831	1.825
d(C_1–O_a)	1.217	1.214	1.236	1.216	1.211	1.231	1.215
d(C_1–O_b)	1.347	1.363	1.345	1.343	1.366	1.353	1.347
d(C_1–C_2)	1.546	1.539	1.528	1.556	1.544	1.518	1.546
d(C_2–C_3)	1.529	1.519	1.537	1.529	1.541	1.529	1.525
d(S–H)	1.353	1.353	1.351	1.354	1.376	1.359	1.352
d(O–H)	0.999	0.975	0.978	0.980	0.978	0.983	0.999
d(C_2–H)	1.102	1.099	1.102	1.103	1.104	1.102	1.103
d(N–H)	1.033	1.030	1.025	1.001	1.025	1.023	1.032
Angle (1)							
a(C_1–C_2–C_3)	110.4	109.9	107.7	109.5	107.1	109.1	111.4
a(C_1–C_2–N)	109.7	107.0	112.2	110.4	113.6	110.6	110.6
a(C_3–C_2–N)	112.4	110.1	109.2	111.3	110.1	111.9	107.7
a(C_2–C_1–O_a)	122.1	122.7	119.5	122.7	123.3	124.5	122.1
a(C_2–C_1–O_b)	116.6	116.8	121.3	116.5	116.2	118.1	117.1
a(O_a–C_1–O_b)	121.2	120.3	119.2	120.8	120.5	117.3	120.8
a(C_2–C_3–S)	105.8	111.3	113.3	113.7	113.0	111.8	113.4
a(C_3–S–H)	97.6	95.5	96.2	94.2	98.4	96.4	95.5

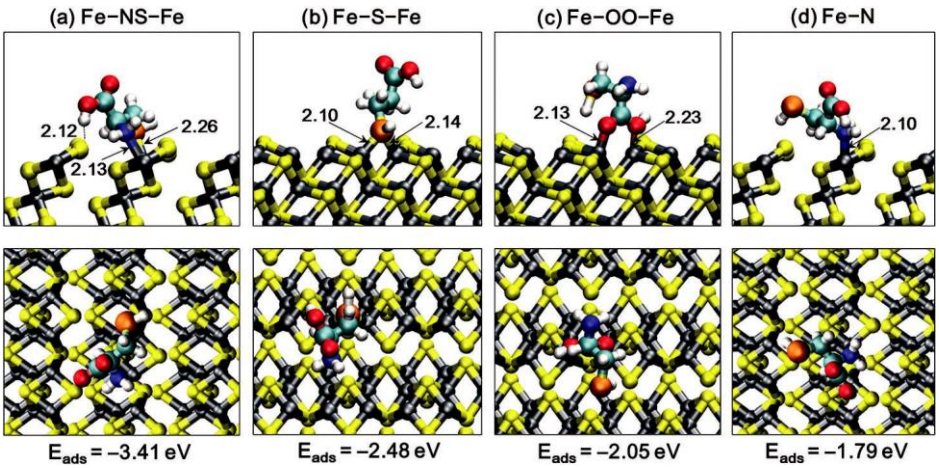

Fig. 7 The lowest-energy adsorption configurations of cysteine on the FeS{111} surface, in side (top) and top (bottom) views. Distances in Angstroms (Å). (colour scheme: Fe = grey, $S_{surface}$ = yellow, $S_{molecule}$ = orange; O, C, N and H are the same as in Fig. 3).

monodentate Fe–N configurations release adsorption energies of 2.05 eV (E_{vdW} = 0.30 eV) and 1.79 eV (E_{vdW} = 0.27 eV) respectively, which are both stronger than the similar configu-ration on the FeS{011} and {100} surfaces. The stronger adsorp-tion calculated for the configurations involving the thiol (–SH) end group on all the surfaces considered suggests that the S orbitals are the driving force for the adsorption of cysteine on FeS surfaces, which is in good agreement with the dominant contribution of the sulfur 3p states to the HOMO, the LUMO, and the DOS at the Fermi level of the cysteine molecule (Fig. 3).

3.6 Electronic properties

In addition to the energies released, the interactions between the cysteine molecule and the FeS surfaces gave rise to electron density redistributions within the FeS–cysteine systems. This is analysed in Fig. 8 by means of projected density of states (PDOS) and differential charge-density difference (Dr) iso-surfaces, which are obtained by subtracting from the electron density of the total FeS–cysteine system both the electron density of the naked FeS surface and that of an isolated cysteine:

$$Dr = r_{surface/cysteine} - (r_{surface} + r_{cysteine}). \quad (6)$$

The atomic positions of the naked FeS surface and the cysteine array (i.e., including the molecule's images in neigh-bouring cells) are considered to be the same as those of the relaxed FeS–cysteine system. In this way, the presentation highlights the electronic structure and bond formation. The insets in Fig. 8 show the iso-surface plot of the electron density difference in the lowest-energy cysteine configurations on the

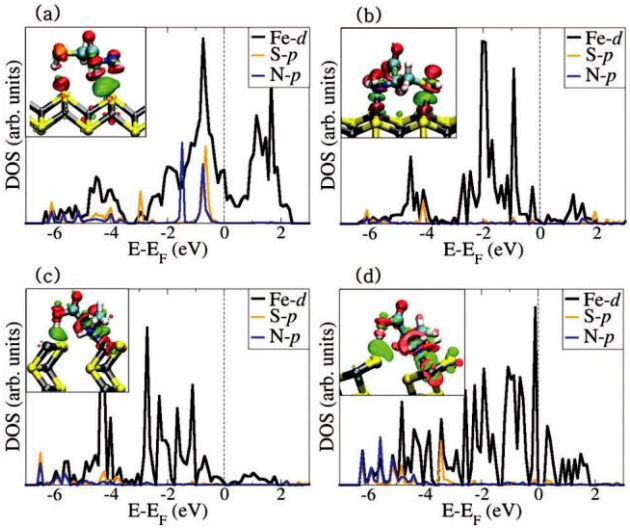

Fig. 8 Partial DOS projected on the interacting surface Fe d-states and on the adsorbed cysteine's S and N p-states at the (a) FeS{001}, (b) FeS{011}, (c) FeS{100}, and (d) FeS{111} surfaces. The insets show the corresponding isosurfaces of the differential charge density, where the green and red contours indicate electron density increase and decrease by 0.02 e Å ^{3}, respectively.

{001}, {011}, {100}, and {111} surfaces. The observed electron density accumulation between the hydrogen and surface sulfur atoms on the {001} surface (Fig. 8a) is characteristic of weak hydrogen-bonded interactions.

An inspection of the isosurface at the {011}, {100}, and {111} surfaces reveals a chemisorption character of cysteine, which leads to charge density accumulation (green contours) around centers of the newly formed Fe–S and Fe–N bonds. We also observe electron density accumulation between the thiol end hydrogen and the {100} and {111} surface S ions, indicative of hydrogen-bonded interactions within these FeS–cysteine com-plexes (Fig. 8(c and d)). The electronic DOS projected on the sulfur and nitrogen p-orbitals of cysteine and the interacting Fe d-orbitals provides further insight into the nature of cysteine interactions with the FeS surfaces. On the {001} surface, we observe only a shift in the cysteine's sulfur and nitrogen p-orbitals towards lower energy levels relative to the gas phase states (Fig. 3d), but there is no hybridisation between them and surface Fe d-states around the Fermi level, as there is no direct chemical bond between these species. In contrast to the {001} surface, adsorption of cysteine on the {011}, {100}, and {111} surfaces reveals a strong hybridization between the sulfur and nitrogen p-orbitals of the cysteine molecule and the d-orbitals of the interacting surface Fe ions, which is consistent with the formation of new Fe–S and Fe–N bonds between the cysteine molecule and the surface Fe sites. The strong hybridization between sulfur and nitrogen p-orbitals of the cysteine molecule and the d-orbitals of the interacting surface Fe atoms is characterized by the disappearance of the S p-states around the Fermi level. While there are local electron rearrangements within the FeS–cysteine systems as shown by the differential charge-density difference iso-surfaces (insets in Fig. 8), the net charge transfer from the FeS surfaces to the cysteine molecule, as estimated by the space partitioning scheme of Bader,[102] is very small (Table 2). The small net charge gained by the cysteine molecule upon adsorption is consistent with the small changes in the structural parameters of the adsorbed molecule compared to the gas phase parameters.

3.7 Vibrational properties

In order to assign the vibrational modes of the adsorbed cysteine molecule, we have computed the wavenumbers of the normal modes for different cysteine adsorption configura-tions, on the FeS surfaces. Shown in Tables 6 and 7 are the calculated vibrational frequencies of the cysteine molecule in the gas phase and in the adsorbed states, respectively. Our calculated vibrational frequencies of the gas phase cysteine molecule compare reasonably well with those reported in earlier theoretical[103–108] and experimental[95,106,109,110] investiga-tions, as shown in Table 5, which ensures the reliability and accuracy of our approximate assignments. The stretching S–H bands of the cysteine molecule on the {001} surface (Table 6) at 2607, 2534, 2617, and 2621 cm ^{1} can be assigned to the flat, SH-end, CH–N-end and O_a-end adsorption configurations, respectively, which are slightly lower than the gas phase stretching S–H band at 2625 cm ^{1}. The small reductions in

Table 5 Molecular vibrational frequencies (in cm ^{1}) of the gas-phase calculated in this work and compared with the available experimental data and earlier theoretical predictions

Assignment	This work	Theory[106]	Theory[107]	Theory[108]	IR[106]	Raman[107,109]
C_3–S stretch	742	666	713	688	—	—
SH bending	952	987	976	—	—	—
CO_2 s-stretch	1107	1389	1372	1374	1377	1397
C_2–H bend	1347	1326	1341	—	—	—
CH_2 bending	1425	1440	1423	1468	1424	1424
NH_2 bending	1596	1577	1538	—	1581	1574
CO_2 as-stretch	1781	1782	1602	—	1645	1644
S–H stretch	2625	2604	2516	2682	2540	2546
C_2–H stretch	2925	2925	3012	2999	—	2970
CH_2 s-stretch	2992	2910	2965	—	—	—
CH_2 as-stretch	3062	2995	3027	—	—	3000
NH_2 s-stretch	3420	3280	—	—	—	—
NH_2 as-stretch	3518	3381	—	—	—	3190
O_b–H stretch	3669	—	—	—	—	—

Table 6 Molecular vibrational frequencies (in cm ^{1}) of adsorbed cysteine on FeS{001} and FeS{011} surfaces

	FeS{001}				FeS{011}			
Assignment	Flat	SH-end	CH–N-end	O_a-end	Fe–NS–Fe	Fe–OO–Fe	Fe–S	Fe–N
C_3–S stretch	715	697	700	699	701	744	754	743
C_1–O_b stretch	1116	1146	1112	1107	1106	1067	1138	1125
C_3–C_2–H bend	1200	1362	1285	1348	1386	1289	1289	1224
CH_2 scissor	1392	1414	1391	1398	1415	1417	1415	1403
NH_2 scissor	1601	1615	1613	1596	1588	1597	1593	1581
C_1–O_a stretch	1795	1751	1765	1755	1784	1637	1765	1780
S–H stretch	2607	2534	2617	2621	2584	2635	2570	2523
C_2–H stretch	2909	2903	2908	2956	2816	2946	2942	3006
CH_2 s-stretch	2962	2998	2960	2988	2981	2994	2992	2936
CH_2 as-stretch	3062	3058	3057	3050	3096	3060	3061	3030
NH_2 s-stretch	3394	3394	3390	3420	3353	3460	3302	3315
NH_2 as-stretch	3482	3474	3478	3517	3423	3611	3632	3413
O_b–H stretch	3508	3257	3517	3695	3626	3632	3404	3317

the stretching S–H bands can be attributed to the hydrogen-bonded interactions with the surface sulfur atoms, which have caused a weakening of the S–H bonds. The stretching O_b–H modes at 3508, 3257, 3517, and 3695 cm ^{1} are assigned to the cysteine adsorbed in the flat, SH-end, CH–N-end and O_a-end adsorption configurations respectively. The NH_2 symmetric and asymmetric stretching frequencies (3394; 3482 cm ^{1}) can be assigned to the lowest-energy flat configuration, whereas the CH_2 symmetric and asymmetric stretching frequencies (2962; 3062 cm ^{1}) are assigned to those on FeS{001}.

For the cysteine interactions with the {011}, {100}, and {111} surfaces, the S–H stretching bands of cysteine at 2584, 2590, and 2583 cm ^{1} are assigned to the lowest-energy adsorption configurations, respectively (Tables 6 and 7). When compared to the gas phase S–H bands at 2625 cm ^{1}, they indicate a softening of the vibrational modes and therefore weakening of the S–H bonds. Similar results were reported from Fourier transform infrared spectroscopy (FT-IR) for the interactions of the thiol groups with minerals and metal surfaces, where the stretching S–H band at 2562 cm ^{1} vanishes.[57–60] The stretching O_b–H modes for the lowest-energy cysteine configurations on the {011}, {100}, and {111} surfaces are observed at 3626, 3622, and 3620 cm ^{1} respectively. Compared to the gas phase stretching O_b–H band at 3669 cm ^{1}, it is worth noting that there is a reduction in the stretching O_b–H modes, which is in agreement with the hydrogen-bonded interactions in these complexes with longer O_b–H bond lengths. We have also observed softening of the symmetric and asymmetric stretching NH_2 modes, (3353; 3423 cm ^{1}), (3343; 3413 cm ^{1}), and (3313; 3411 cm ^{1}), respec-tively, assigned to the lowest-energy adsorption configurations on the {011}, {100}, and {111} surfaces.

3.8 Equilibrium crystal morphologies

Wulff[75] and Gibbs[94] showed that equilibrium morphologies of minerals can be obtained from their surface energies and we investigated whether the morphology of mackinawite is changed by the adsorption of cysteine onto its surfaces, by comparing the morphology of the clean material with that calculated from the surface energies after adsorption of cysteine. Lattice dynamics simulations have shown that the contribution of the excess entropy term to the surface free energy is small compared to the enthalpy term, as the differences between the entropies of the bulk and the surface are small and hence for solid surfaces the surface energy is a close approximation of the surface free energy.[111] Thus, the surface energies can be assumed to deter-mine the equilibrium morphology of the crystal. This approach has been employed in the calculation of the effect of surface adsorbates on the thermodynamic morphologies of many different

Table 7 Molecular vibrational frequencies (in cm ^{1}) of adsorbed cysteine on FeS{100} and FeS{111} surfaces

	FeS{100}			FeS{111}			
Assignment	Fe–NS–Fe	Fe–N	Fe–O	Fe–NS–Fe	Fe–S–Fe	Fe–OO–Fe	Fe–N
C_3–S stretch	700	740	761	693	754	751	741
C_1–O_b stretch	1101	1121	1083	1106	1138	1071	1117
C_3–C_2–H bend	1387	1234	1295	1383	1289	1290	1247
CH_2 scissor	1413	1407	1423	1418	1415	1418	1410
NH_2 scissor	1589	1579	1598	1590	1593	1587	1583
C_1–O_a stretch	1779	1776	1630	1780	1765	1633	1757
S–H stretch	2590	2533	2637	2583	2570	2615	2538
C_2–H stretch	2816	3013	2954	2815	2942	2953	2973
CH_2 s-stretch	2979	2926	2990	2975	2992	2987	2920
CH_2 as-stretch	3063	3023	3063	3059	3061	3060	3017
NH_2 s-stretch	3343	3314	3467	3313	3302	3457	3312
NH_2 as-stretch	3413	3410	3610	3411	3632	3603	3411
O_b–H stretch	3622	3319	3632	3620	3404	3601	3307

Table 8 Calculated surface energies of pure mackinawite before (g_r) and after cysteine adsorption ($g_{cysteine}$)

Surface	g_r (J m^{-2})	$g_{cysteine}$ (J m^{-2})
{001}	0.19	0.21
{011}	0.95	0.72
{100}	1.04	0.81
{111}	1.51	0.76

materials, e.g. oxides, carbonates, phosphates and sulfides,[111–116] where good agreement was obtained with experiment. We have therefore employed the same approach here to obtain the morphology of the FeS crystal and investigate the effect of cysteine adsorption on the expression of different low-index surfaces in the resulting morphology, using the calculated surface energies listed in Table 8. The order of increasing surface energies, and therefore decreasing stability of the dry FeS surfaces, was determined to be {001} o {011} o {100} o {111},[34] which is consistent with the results obtained from the selected area electron diffraction (SAED) analysis of FeS nanocrystals.[90] The {001} surface is by far the most stable surface of FeS because its creation only involves breaking the weak vdW interactions between the sulfide layers, with negligible relaxation of the surface species. Except for the {001} surface, all the other FeS surfaces considered were stabilised considerably by the adsorption of cysteine (Table 8). The stabilisation of the {011}, {100}, and {111} surfaces compared to the {001} surface can be attributed to the strong binding of cysteine to these surfaces, whereas on the {001} surface it is only weakly physisorbed owing to repulsive interactions between the negatively charged S ions terminating the surface and the adsor-bate's O, S and N ions. The strength of cysteine adsorption on various FeS surfaces is consistent with the trend generally observed for the thermodynamic stabilities of the surfaces, where the less stable surfaces are more reactive towards adsorbing species.[117] The {001} surface, however, remains the most stable surface after adsorption of cysteine, with a surface energy of 0.21 J m^{-2}.

Shown in Fig. 9a is the morphology of the clean FeS crystal, which reveals thin and tabular crystal morphology, with the facet corresponding to the {001} orientation enclosing the largest area. The edges of the clean FeS crystals are formed by the {011}, {100}, and {111} facets. Similar observations were made from high resolution transmission electron microscope (HRTEM) examination of FeS aggregates.[90] Since the surface energies change as an effect of cysteine adsorption, the mor-phology is altered as shown in Fig. 9b. As expected the stronger binding of the cysteine molecule to the {011}, {100}, and {111} surfaces, rather than the {001} facet, causes these reactive surfaces to become more prominent in the crystal morphology in the presence of cysteine, owing to their decreased surface energies, and therefore increased stability. Crystal growth is hindered in the {011}, {100}, and {111} orientations compared to the {001} orientation, which interacts weakly with cysteine. As such, the FeS moiety grows much more rapidly perpendi-cular to the {001} surface, rather than extending it horizontally. In essence, the {001} surface becomes less dominant in morpho-

logy with respect to other surfaces, as is found in many crystals grown in the presence of growth-modifying moieties.[118,119] It should be noted, however, that these results are based on the adsorption of only one cysteine molecule on each FeS surface simulated cell, whereas increasing the cysteine coverage on the surfaces may conceivably lead to further expression of the reactive surfaces in the morphology. These results are in agree-ment with experimental results, which showed that cysteine stabilizes the surfaces of FeS nanoparticles during synthesis, thereby modifying the shape and size as revealed by scanning electron microscopy (SEM).[46] The greater expression of the more reactive surfaces in the FeS particle grown in the presence of cysteine or similar surfactants is expected to enhance the catalytic performance of the FeS nanoparticles.

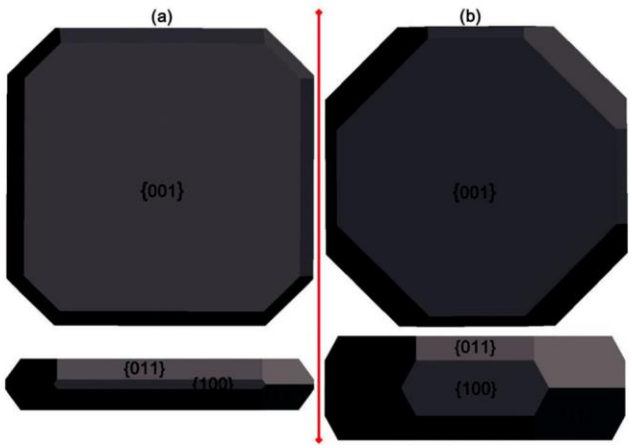

Fig. 9 Equilibrium crystal morphology of (a) clean FeS and (b) cysteine modified FeS.

4. Summary and conclusions

We have studied the adsorption of the amino acid cysteine onto the low-index {001}, {011}, {100}, and {111} surfaces of FeS, by means of dispersion-corrected density functional theory calculations. We found that the strength of adsorption of cysteine onto the low-index FeS surfaces is related to the stability of different surfaces, where it adsorbs most strongly onto the least stable FeS{111} surface and most weakly onto the most stable FeS{001} surface; the adsorption energy decreases in the order FeS{111} 4 FeS{100} 4 FeS{011} 4 FeS{001}. Hydrogen-bonded and vdW interactions are found to play important roles in stabilizing the cysteine molecule on the {001} surface, whereas on the {011}, {100}, and {111} surfaces, cysteine is anchored via direct Fe–S and Fe–N chemical bonds. Consistent with the formation of new bonds between the surface and cysteine, we observed electron density accumulation around centers of the newly formed bonds. Analyses of the electronic structures also reveal strong hybridisation between the sulfur and nitrogen p-orbitals of the cysteine molecule and the d-orbitals of the interacting surface Fe ions, which gave rise to small net charge transfer from the surface to the adsorbed cysteine.

The stabilities of the low-index mackinawite surfaces are shown to be affected by the adsorption of cysteine. Except for the {001} surface, all the other FeS surfaces considered were stabilised considerably by the adsorption of cysteine, especially the most reactive {111} surface. Since the surface energies change as an effect of cysteine adsorption, the equilibrium morphology is altered. The strong adsorption of the cysteine molecule onto the {011}, {100}, and {111} surfaces, in preference to the {001} facet, changes the FeS crystal shape, with the reactive surfaces becoming more expressed in the equilibrium morphology. The greater expression of the more reactive surfaces in the FeS nanocrystals grown in the presence of cysteine or similar surfac-tants should give rise to an enhancement of the catalytic perfor-mance of the FeS nanoparticles. The structural parameters, vibrational frequency assignments and the electronic properties from this work may be relevant for the investigation of self-assembled cysteine monolayers, dimer-adsorption, and other higher coverage structures in future works.

Acknowledgements

We acknowledge the Netherlands Foundation for Fundamental Research on Matter (FOM) for funding (Grant No. 13CO26-2). This work made use of the facilities of ARCHER (http://www.archer.ac.uk), the UK's national supercomputing service via our membership of the UK's HEC Materials Chemistry Consortium, which is funded by EPSRC (EP/L000202).

References

1 Z. A. Peng and X. Peng, J. Am. Chem. Soc., 2001, 123, 1389–1395.
2 A. R. Tao, S. Habas and P. Yang, Small, 2008, 4, 310–325. 3 Y. W. Jun, Y. M. Huh, J. S. Choi, J.-H. Lee, H.-T. Song, S. Kim, S. Yoon, K.-S. Kim, J. S. Shin and J. Cheon, J. Am. Chem. Soc., 2005, 127, 5732–5733.
4 D. Kimberly, T. Dhanasekaran, Z. Zhang and D. Meisel, J. Am. Chem. Soc., 2002, 124, 2312–2317.
5 P. Alivisatos, Science, 1996, 271, 933–937.
6 J. L. Marignier, J. Belloni, M. O. Delcourt and J. P. Chevalier, Nature, 1985, 317, 344–345.
7 F. Zaera, ChemSusChem, 2013, 6, 1797–1820.
8 T. S. Ahmadi, Z. L. Wang, T. C. Green, A. Henglein and M. A. Elsayed, Science, 1996, 272, 1924–1926.
9 W. Huynh, X. Peng and A. P. Alivisatos, Adv. Mater., 1999, 11, 923–927.
10 M. C. Schlamp, X. G. Peng and A. P. Alivisatos, J. Appl. Phys., 1997, 82, 5837–5842.
11 H. Mattoussi, L. H. Radzilowski, B. O. Dabbousi, E. L. Thomas, M. G. Bawendi and M. F. Rubner, J. Appl. Phys., 1998, 83, 7965–7974.
12 M. Bruchez, M. Moronne, P. Gin, S. Weiss and A. P. Alivisatos, Science, 1998, 281, 2013–2016.
13 W. C. W. Chan and S. M. Nie, Science, 1998, 281, 2016–2018.
14 T.-D. Nguyen, Nanoscale, 2013, 5, 9455–9482.
15 C. Burda, X. Chen, R. Narayanan and M. A. El-Sayed, Chem. Rev., 2005, 105, 1025–1102.
16 L. Manna, E. C. Scher and A. P. Alivisatos, J. Cluster Sci., 2002, 13, 521–532.
17 S. Kumar and T. Nann, Small, 2006, 2, 316–329.
18 Y. Yin and A. P. Alivisatos, Nature, 2005, 437, 664–670.
19 J. Perez-Juste, I. Pastoriza-Santos, L. M. Liz-Marzan and P. Mulvaney, Coord. Chem. Rev., 2005, 249, 1870–1901.
20 R. A. Sperling and W. J. Parak, Philos. Trans. R. Soc., A, 2010, 368, 1333–1383.
21 L. Samad, M. Caba´n-Acevedo, M. J. Shearer, K. Park, R. J. Hamers and S. Jin, Chem. Mater., 2015, 27, 3108–3114.
22 Y.-Y. Lin, D.-Y. Wang, H.-C. Yen, H.-L. Chen, C.-C. Chen, C.-M. Chen, C.-Y. Tang and C.-W. Chen, Nanotechnology, 2009, 20, 405207.
23 Y. Bi, Y. Yuan, C. L. Exstrom, S. A. Darveau and J. Huang, Nano Lett., 2011, 11, 4953–4957.
24 J. Puthussery, S. Seefeld, N. Berry, M. Gibbs and M. Law, J. Am. Chem. Soc., 2011, 133, 716–719.
25 B. Wu, H. Song, J. Zhou and X. Chen, Chem. Commun., 2011, 47, 8653–8655.
26 Z. Hu, Z. Q. Zhu, F. Y. Cheng, K. Zhang, J. B. Wang, C. C. Chen and J. Chen, Energy Environ. Sci., 2015, 8, 1309–1316.
27 Y. Yamaguchi, T. Takeuchi, H. Sakaebe, H. Kageyama, H. Senoh, T. Sakai and K. Tatsumi, J. Electrochem. Soc., 2010, 157, A630–A635.
28 A. Paolella, C. George, M. Povia, Y. Zhang, R. Krahne, M. Gich, A. Genovese, A. Falqui, M. Longobardi, P. Guardia, T. Pellegrino and L. Manna, Chem. Mater., 2011, 23, 3762–3768.
29 Y. Shao-Horn, S. Osmialowski and Q. C. Horn, J. Electrochem. Soc., 2002, 149, A1499–A1502.
30 M. Feng, Y. Lu, Y. Yang, M. Zhang, Y.-J. Xu, H.-L. Gao, L. Dong, W.-P. Xu and S.-H. Yu, Sci. Rep., 2013, 3, 2994.
31 C.-H. Lai, M.-Y. Lu and L.-J. Chen, J. Mater. Chem., 2012, 22, 19–30.
32 A. Roldan, N. Hollingsworth, A. Roffey, H.-U. Islam, J. B. M. Goodall, C. R. A. Catlow, J. A. Darr, W. Bras, G. Sankar, K. B. Holt, G. Hogarth and N. H. de Leeuw, Chem. Commun., 2015, 51, 7501.
33 N. Y. Dzade, A. Roldan and N. H. de Leeuw, J. Chem. Phys., 2016, 144, 174704.
34 N. Y. Dzade, A. Roldan and N. H. de Leeuw, Phys. Chem. Chem. Phys., 2014, 16, 15444–15456.
35 A. Roldan and N. H. de Leeuw, Catalytic water dissociation by greigite Fe_3S_4 surfaces: density functional theory study, Proc. R. Soc. A, 2016, 472, 20160080.
36 J. B. Varley, H. A. Hansen, N. L. Ammitzbøll, L. C. Grabow, A. A. Peterson, J. Rossmeisl and J. K Nørskov, ACS Catal., 2013, 3, 2640–2643.
37 G. Cody, N. Boctor, J. Brandes, T. Filley, R. Hazen and H. Yoder, Geochim. Cosmochim. Acta, 2004, 68, 2185–2196.
38 Z. He, S. H. Yu, X. Zhou, X. Li and J. Qu, Adv. Funct. Mater., 2006, 16, 1105–1111.
39 D. W. Wang, Q. H. Wang and T. M. Wang, CrystEngComm, 2010, 12, 755–761.

40 P. V. Vanitha and P. O'Brien, J. Am. Chem. Soc., 2008, 130, 17256–17257.
41 K. Ramasamy, M. A. Malik, M. Helliwell, F. Tuna and P. O'Brien, Inorg. Chem., 2010, 49, 8495–8503.
42 W. O. Bae, R. Abdullah, D. V. Henderson and R. K. Mehra, Biochem. Biophys. Res. Commun., 1997, 237, 16.
43 W. Bae and R. K. Mehra, J. Inorg. Biochem., 1998, 69, 33–43.
44 W. O. Bae, R. Abdullah and R. K. Mehra, Chemosphere, 1998, 37, 363–385.
45 W. W. Yu, Y. A. Wang and X. G. Peng, Chem. Mater., 2003, 15, 4300–4308.
46 M. R. M. Chaves, K. T. Valsaraj, R. D. DeLaune, R. P. Gambrell and P. M. Buchler, in Sediment Transport, ed. S. S. Ginsberg, InTech, 2011, DOI: 10.5772/15041.
47 A. R. Lennie, S. A. T. Redfern, P. F. Schofield and D. J. Vaughan, Mineral. Mag., 1995, 59, 677–683.
48 R. A. Berner, Science, 1962, 137, 669.
49 G. Wa¨chtersha¨user, Prog. Biophys. Mol. Biol., 1992, 58, 85–201.
50 G. Wa¨chtersha¨user, Origins Life Evol. Biospheres, 1990, 20, 173–176.
51 C. Huber and G. Wa¨chtersha¨user, Science, 1998, 281, 670–672.
52 Q. Chi, J. Zhang, J. U. Nielsen, E. P. Friis, I. Chorkendorff, G. W. Canters, J. E. T. Andersen and J. Ulstrup, J. Am. Chem. Soc., 2000, 122, 4047–4055.
53 S. M. C. Ritchie, K. E. Kissick, L. G. Bachas, S. K. Sikdar, C. Parikh and D. Bhattacharyya, Environ. Sci. Technol., 2001, 35, 3252–3258.
54 T. Baas, L. Gamble, K. D. Hauch, D. G. Castner and T. Sasaki, Langmuir, 2002, 18, 4898–4902.
55 A.-C. Liu, D. Chen, C.-C. Lin, H.-H. Chou and C. Chen, Anal. Chem., 1999, 71, 1549–1552.
56 Z. He, S. H. Yu, X. Zhou, X. Li and J. Qu, Adv. Funct. Mater., 2006, 16, 1105–1111.
57 M. F. Brigatti, C. Luoli, S. Montorsi and L. Poppi, Clays Clay Miner., 1999, 47, 664–667.
58 S. Aryal, B. K. C. Remant, N. Dharmaraj, N. Bhattarai, C. H. Kim and H. Y. Kim, Spectrochim. Acta, Part A, 2006, 63, 160–163.
59 L. O. Benetoli, C. M. de Souza, K. da Silva, I. G. de Souza Jr, H. de Santana, A. Paesano Jr, A. C. Costa, C. T. B. V. Zaia and D. A. M. Zaia, Origins Life Evol. Biospheres, 2007, 37, 479–493.
60 H. de Santana, A. Paesano Jr, A. C. da Costa, E. Di Mauro, I. G. de Souza Jr, F. F. Ivashita, C. M. de Souza, C. T. B. V. Zaia and D. A. M. Zaia, Amino Acids, 2010, 38, 1089–1099.
61 D. A. M. Zaia, Amino Acids, 2004, 27, 113–118.
62 V. A. Basiuk, Adsorption of biomolecules at silica, Encyclopaedia of surface and colloid science, Marcel Dekker Inc., New York, 2002, pp. 277–293.
63 J. F. Lambert, Origins Life Evol. Biospheres, 2008, 38, 211–242.
64 A. P. Vieira, G. Berndt, I. G. de Souza Jr, E. Di Mauro, A. Paesano Jr, H. de Santana, A. C. S. da Costa, C. T. B. V. Zaia and D. A. M. Zaia, Amino Acids, 2011, 40, 205–214.
65 J. Bebie´ and M. A. A. Schoonen, Geochem. Trans., 2000, 1, 47–53.
66 L. O. B Benetoli, C. M. D. de Souza, K. L. da Silva, I. G. de Souza Jr, H. de Santana, A. Paesano Jr, A. C. S. da Costa, C. T. B. V. Zaia and D. A. M. Zaia, Origins Life Evol. Biospheres, 2007, 37, 479–493.
67 J.-F. Lambert, L. Stievano, I. Lopes, M. Gharsallah and L. Piao, Planet. Space Sci., 2009, 57, 460–467.
68 V. A. Basiuk and T. Y. Gromovoy, Colloids Surf., A, 1996, 118, 127–140.
69 M. Meng, L. Stievano and J.-F. Lambert, Langmuir, 2004, 20, 914–923.
70 E. M. Marti, Ch. Methivier and C. M. Pradier, Langmuir, 2004, 20, 10223–10230.
71 S. Stewart and P. M. Fredericks, Spectrochim. Acta, Part A, 1999, 55, 1641–1660.
72 R. Di Felice, A. Selloni and E. Molinari, J. Phys. Chem. B, 2003, 107, 1151–1156.
73 A. Nilsson and L. G. M. Pettersson, Surf. Sci. Rep., 2004, 55, 49–167.
74 T. Bligaard and J. K. Nørskov, in Chemical Bonding at Surfaces and Interfaces, ed. A. Nilsson, L. G. M. Petterson and J. K. Nørskov, Elsevier, Amsterdam, 1st edn, 2008.
75 G. Wulff, Z. Krystallogr. Miner., 1901, 34, 449–530.
76 G. Kresse, Phys. Rev. B: Condens. Matter Mater. Phys., 1999, 59, 1758–1775.
77 G. Kresse and J. Furthmu¨ller, Phys. Rev. B: Condens. Matter Mater. Phys., 1996, 54, 11169–11186.
78 G. Kresse and J. Furthmu¨ller, Comput. Mater. Sci., 1996, 6, 15–50.
79 S. Grimme, J. Comput. Chem., 2006, 27, 1787–1799.
80 N. Y. Dzade, A. Roldan and N. H. de Leeuw, J. Chem. Phys., 2013, 139, 124708.
81 J. P. Perdew and A. Zunger, Phys. Rev. B: Condens. Matter Mater. Phys., 1981, 23, 5048–5079.
82 J. P. Perdew, J. A. Chevary, S. H. Vosko, K. A. Jackson, M. R. Pederson, D. J. Singh and C. Fiolhais, Phys. Rev. B: Condens. Matter Mater. Phys., 1992, 46, 6671.
83 P. E. Blo¨chl, Phys. Rev. B: Condens. Matter Mater. Phys., 1994, 50, 17953–17979.
84 G. Kresse and D. Joubert, Phys. Rev. B: Condens. Matter Mater. Phys., 1999, 59, 1758–1775.
85 H. J. Monkhorst and J. D. Pack, Phys. Rev. B, 1976, 13, 5188–5192.
86 A. J. Devey, R. Grau-Crespo and N. H. de Leeuw, J. Phys. Chem. C, 2008, 112, 10960–10967.
87 D. J. Vaughan and M. S. Ridout, J. Inorg. Nucl. Chem., 1971, 33, 741–746.
88 A. Subedi, L. J. Zhang, D. J. Singh and M. H. Du, Phys. Rev. B: Condens. Matter Mater. Phys., 2008, 78, 134514.
89 J. Brgoch and G. J. Miller, J. Phys. Chem. A, 2012, 116, 2234–2243.
90 H. Ohfuji and D. Rickard, Earth Planet. Sci. Lett., 2006, 241, 227–233.

91 G. W. Watson, E. T. Kelsey, N. H. de Leeuw, D. J. Harris and S. C. Parker, J. Chem. Soc., Faraday Trans., 1996, 92, 433–438.
92 P. W. Tasker, J. Phys. C: Solid State Phys., 1979, 12, 4977–4984.
93 S. Baroni, S. de Gironcoli, A. Dal Corso and P. Giannozzi, Rev. Mod. Phys., 2001, 73, 515–562.
94 J. W. Gibbs, Collected Works, Longman, New York, 1928.
95 S. Gunasekaran, A. Bright, T. S. Renuga Devi, R. Arunbalaji, G. Anand, J. Dhanalakshmi and S. Kumaresan, Arch. Phys. Res., 2010, 1, 12–26.
96 C. Kemnitz, ''Chemoffice ultra 10'' Trial version, 2002.
97 C. H. Go¨rbitz and B. Dalhus, Acta Crystallogr., Sect. C: Cryst. Struct. Commun., 1996, 52, 1756–1759.
98 K. A. Kerr, J. P. Ashmore and T. F. Koetzle, Acta Crystallogr., Sect. B: Struct. Sci., 1975, 31, 2022–2026.
99 M. Yang, S. S. Stipp and J. Harding, Cryst. Growth Des., 2008, 8, 4066–4074.
100 T. Hayashi, Y. Morikawa and H. Nozoye, J. Chem. Phys., 2001, 114, 7615.
101 M. C. Vargas, P. Giannozzi, A. Selloni and G. Scoles, J. Phys. Chem. B, 2001, 105, 9509.
102 G. Henkelman, A. Arnaldsson and H. Jonsson, Comput. Mater. Sci., 2006, 36, 354–360.
103 P. Tarakeshwar and S. Manogaran, THEOCHEM, 1998, 429, 31–40.
104 H. Susi, D. M. Byler and W. V. Gerasimowicz, J. Mol. Struct., 1983, 102, 63–69.
105 P. Tarakeshvar and S. Manogaran, Spectrochim. Acta, Part A, 1995, 51, 925–928.
106 A. Pawlukojc´, J. Leciejewicz, A. J. Ramirez-Cuesta and J. Nowicka-Scheibe, Spectrochim. Acta, Part A, 2005, 61, 2474–2481.
107 S. F. Parker, Chem. Phys., 2013, 424, 75–79.
108 C. Jing and Y. Fang, Chem. Phys., 2007, 332, 27–32.
109 J. K. Lim and S.-W. Joo, J. Electroanal. Chem., 2007, 605, 68–72.
110 V. S. Minkov, S. V. Goryainov, E. V. Boldyreva and C. H. Go¨rbitz, J. Raman Spectrosc., 2010, 41, 1458–1468.
111 D. Mkhonto and N. H. de Leeuw, J. Mater. Chem., 2002, 12, 2633–2642.
112 N. H. de Leeuw and S. C. Parker, J. Am. Ceram. Soc., 1999, 82, 3209–3216.
113 N. H. de Leeuw and T. G. Cooper, Geochim. Cosmochim. Acta, 2007, 71, 1655–1673.
114 D. Santos-Carballal, A. Roldan, R. Grau-Crespo and N. H. de Leeuw, Phys. Chem. Chem. Phys., 2014, 16, 21082–21097.
115 S. Haider, A. Roldan and N. H. de Leeuw, J. Phys. Chem. C, 2014, 118, 1958–1967.
116 N. H. de Leeuw and S. C. Parker, J. Phys. Chem. B, 1998, 102, 2914–2922.
117 N. H. de Leeuw and J. A. L. Rabone, CrystEngComm, 2007, 9, 1178–1186.
118 T. G. Cooper and N. H. de Leeuw, Mol. Simul., 2002, 28, 539–556.
119 T. G. Cooper and N. H. de Leeuw, J. Cryst. Growth, 2006, 294, 137–149.